Leu-Enkephalin Lipid Prodrug Nanoparticles: Relationship between Nanoparticles' Structure, Interaction with Bovine Serum Albumin, and Analgesic Activity

Sinda Lepetre-Mouelhi, Alexandre Da Silva, Lucas Prades, Jiao Feng, Frank Wien, Patrick Couvreur, Fabienne Testard, Frédéric Gobeaux

Leu-enkephalin lipid prodrug nanoparticles: relationship between nanoparticles' structure, interaction with Bovine Serum Albumin and analgesic activity

Sinda LEPETRE-MOUELHI (1), Fréderic GOBEAUX (2,*), Alexandre DA SILVA(1), Lucas PRADES (1), Jiao FENG (1), Frank WIEN(3), Patrick COUVREUR(1,*), Fabienne TESTARD(2)

(1) Institut Galien Paris-Saclay, UMR CNRS 8612, Université Paris-Saclay, Orsay Cedex, France.
(2) Université Paris-Saclay, CEA Saclay, CNRS, NIMBE, UMR 3685, LIONS, 91191 Gif-Sur-Yvette Cedex, France
(3) SOLEIL Synchrotron, Saint Aubin 91190, France

KEYWORDS (Word Style "BG_Keywords"). Nanomedicines, Leu-enkephalin, squalene, self-assembling nanoparticles, supramolecular structure, SRCD, SAXS/WAXS, CryoTEM, plasma proteins.

Corresponding authors:
Patrick COUVREUR <patrick.couvreur@universite-paris-saclay.fr> and Frédéric GOBEAUX <Frederic.GOBEAUX@cea.fr>

ABSTRACT (Word Style "BD_Abstract").:

Recently, we proposed in a paper a novel nanomedicine approach, based on a versatile bioconjugation linkage (Amide, Diglycolate or Acylal) between the Leu-enkephalin (LENK), an endogenous neuropeptide, and the squalene (SQ), a natural and biocompatible lipid. The nanoformulation of the resulting bioconjugates allowed the specific delivery of LENK into inflamed tissues for efficient pain control, after their intravenous administration. However, the variability of the analgesic profiles exhibited by the three types of LENK-SQ nanoparticles (NPs) remains not well understood. This study investigates the influence of the LENK-SQ NPs composition on their supramolecular organization and their interaction with blood proteins. To achieve this objective, a physico-chemical study was carried out using complementary techniques such as Dynamic Light Scattering (DLS), Small/Wide Angle X-Ray and Neutron Scattering (SAXS-WAXS and SANS), as well as Circular Dichroism (CD). This study brought together some important information allowing to shed light on the crucial link between nanoparticles' structure, stability and their analgesic activity.

1. Introduction

Nanotechnology represents a very smart approach for the targeted delivery, controlled release and protection from rapid metabolization of therapeutic agents.[1] However, the understanding of the impact of the physico-chemical properties of the nanoparticles (NPs) on their *in vivo* and *in vitro* biological activity is still challenging.[2] The nanoformulation of drugs gives rise to a complex equilibrium between the *in vivo* behavior of the NPs (in terms of stability, surface area and functionalization, specific interaction with plasma proteins and other biological compounds...) and the biopharmaceutic profile and therapeutic efficacy of the encapsulated drugs (pharmacokinetic, pharmacodynamic and biodistribution profiles).

In 2006, Couvreur *et al.* developed a new nanomedicine platform based on squalene, a biocompatible and biodegradable lipid (which was already commonly used as an adjuvant of parenteral emulsions for drug and vaccine delivery[3–5]), used as vectorization agent.[6] The squalene was coupled to a drug through a chemical bio-cleavable linkage and the resulting bioconjugates, which are prodrugs, showed the ability to self-assemble into nanoparticles of around 100 nm diameter with a liquid crystalline internal structure. The so-called "squalenoylation" nanotechnology has been initially proposed for metabolically sensitive small molecules and was further extended to macromolecules such as SiRNA.[7–9] In general, the squalene-based NPs allowed protection of the drugs with a better targeting *in vivo*, thus enhancing their pharmacological activity and reducing their toxicity and side effects.[7,10]

More recently, the *squalenoylation* was applied to Leu-enkephalin, an endogenous neuropeptide, playing an important role in pain regulation.[11]

Indeed, currently, opioids and opioid derivatives are a class of drugs used for the management and treatment of moderate to severe pain in clinics. By preferentially binding to μ-opioid receptors, these painkiller agonists or antagonists are, however, often associated with severe side effects, such as tolerance and dependence with some risks of respiratory depression and death.[12] In this context, with a ten-fold higher affinity towards δ-opioid receptors versus μ-opioid receptors, enkephalin neuropeptides appear as a promising alternative to these addictive opioid drugs.[13] In fact, compared to μ-opioid receptor agonists, δ-opioid receptor ligands have a much lower abuse potential,[14–17] thus generating fewer side effects. However, the clinical use of endogenous neuropeptides has historically been limited because of pharmacokinetic issues including rapid plasma metabolization.[18,19]

Thus, by using the *squalenoylation* approach, we could provide protection to the Leu-enkephalin neuropeptide after intravenous administration and enabled the targeted delivery

into inflamed tissues for pain management.[11] And it was demonstrated that after conjugation with squalene (SQ), the otherwise rapidly metabolized Leu-enkephalin (LENK) became clinically usable. Of note, the Leu-enkephalin (LENK) was chemically coupled to the squalene (SQ) derivative either directly through an amide bond or by using diglycolate or acylal spacers (Scheme 1).

The three resulting LENK-SQ bioconjugates, which are prodrugs, showed the ability to self-assemble spontaneously in water to form nanoparticles with diameters varying from 75 to 122 nm diameter. The two spacers were introduced between LENK and SQ to modulate the LENK release from the LENK-SQ nanoparticles (NPs) *in vivo*. It was observed that these squalene-based NPs enabled the neuropeptide to gain in pharmacological efficacy by displaying a notable antihyperalgesic effect, lasting longer than after treatment with morphine. Pain sensitivity was assessed by measuring the paw withdrawal latencies (PWLs) in response to a hot stimulus on the inflamed hind paw of rats (Figure 1).

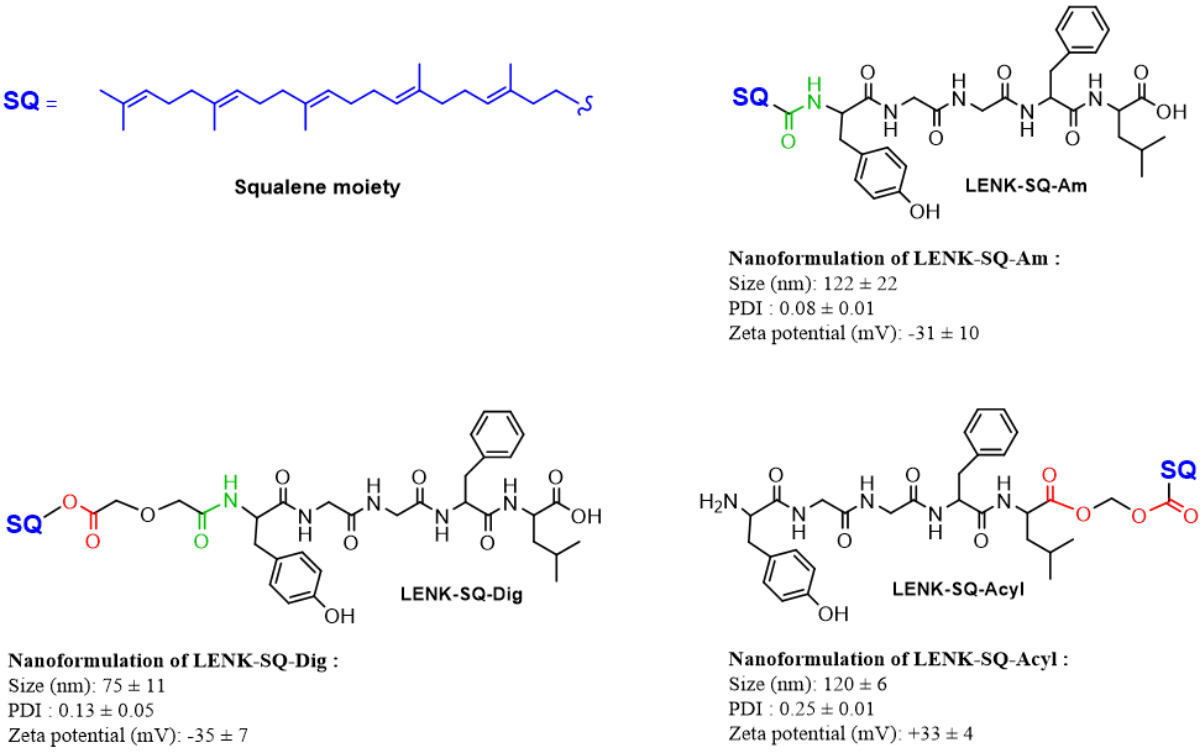

Scheme 1. Chemical structures of the LENK-SQ bioconjugates. (1) Leu-enkephalin-squalene with amide linker (LENK-SQ Am), (2) Leu-enkephalin-squalene with diglycolate linker (LENK-SQ Dig), and (3) Leu-enkephalin-squalene with acylal linker (LENK-SQ Acyl). The amide bond is represented in green and the ester bond in red. The NPs were prepared at a concentration of 4 mg/ml in 5% dextrose solution.[11]

Interestingly, the three LENK-SQ NPs exhibited different analgesic profiles, thus allowing to manage a broad spectrum of pain types (in terms of intensity and duration). The anti-nociceptive effect was explained by the specific accumulation of the LENK-SQ NPs in the inflamed paw triggered by a more leaky vasculature (Figure 1B), thus bypassing the central nervous system including the brain, known as the "reward pathway".[20]

It is noteworthy that previous *in vitro* experiments showed that the release kinetics of LENK peptide from the 3 LENK-SQ NPs after incubation in serum (Figure 2) were not correlated with the observed *in vivo* analgesic profiles (Figure 1A).[11] For instance, the LENK-SQ Am NPs, which didn't show any *in vitro* release of the peptide – unlike the other two LENK-SQ NPs –, exhibited on the contrary a faster and higher anti-nociceptive efficacy but with a shorter duration. On the other hand, the LENK-SQ Acyl NPs, providing rapid release of the LENK peptide *in vitro*, exhibited nearly the same anti-hyperalgesic profile than the LENK-SQ-Dig NPs, with prolonged effect (Figure 1).[11]

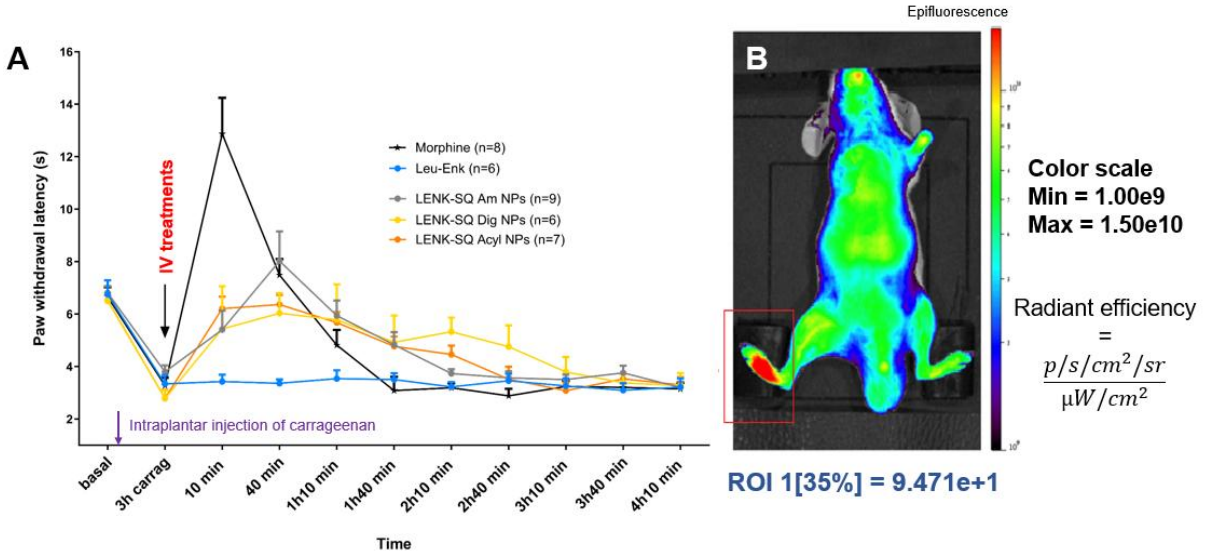

Figure 1. Analgesic profiles of LENK-SQ NPs in comparison with morphine and free LENK (left) and IVIS Lumina scan after intravenous administration of fluorescent LENK-SQ Am NPs (right). **(A)** Measurement of Paw Withrawal Latencies (PWL) in λ-carrageenan–treated rats (in seconds, means ± SEM of independent determinations in five to nine animals per group) using the Hargreaves test, after the administration of LENK-SQ NPs (in grey for LENK-SQ Am, in yellow for LENK-SQ Dig, in orange for LENK-SQ Acyl), Morphine (in black), Leu-enkephalin (in blue). **(B)** Selective accumulation of DiD-fluorescently labelled LENK-SQ Am NPs in the inflamed paw (in red) and not in the healthy contralateral paw. No fluorescence observed in the brain (adapted from 14).

Moreover, it is also interesting to note that according to the site of bioconjugation of SQ (on N- or C- terminal site of the LENK peptide), a net positive or negative surface charge (zeta potential) was observed onto the surface of the NPs (Scheme 1). These parameters are important to consider because it is well known that the composition of protein coronas dramatically influences the colloidal stability of the NPs *in vivo*, and consequently the

biological responses, including NPs pharmacokinetics, biodistributions, and pharmacological efficacy. But still more importantly, the nature of the bioconjugates may result in dramatically different supramolecular architectures with various internal organizations and shapes of NPs including lamellar, hexagonal, cubic and toroidal, as well as ribbons, vesicles, helical strands, spherical or wormlike micelles and amorphous structures.[21–25] These parameters represent also a key factor that determine the diffusion of enzymes into the nanoparticle core and consequently the kinetic release of the drug from the NPs.

Thus, the aim of the current study was to shed light on how the chemical linkage between the LENK and the SQ (i.e., direct amide (Am) bond, diglycolate (Dig) or acylal (Acyl) spacers) could impact the physico-chemical properties of the NPs (in terms of supramolecular organization and interaction with plasma proteins) and consequently influence the resulting analgesic profiles. Noteworthy, only few studies have been carried out to investigate the effect of plasma proteins on the integrity of liquid crystalline nanoparticles[26,27,28] and in particular for SQ NPs.[29,30]

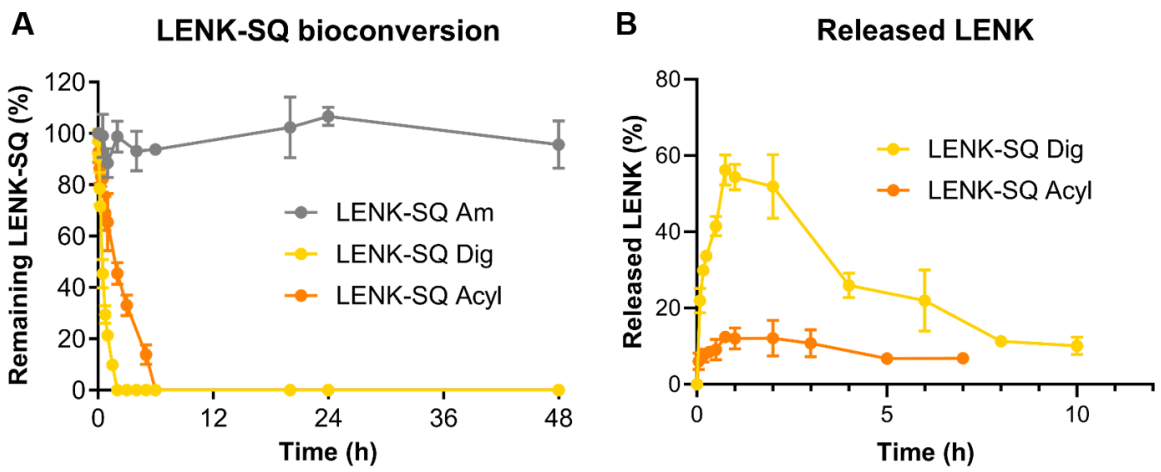

Figure 2. Bioconversion of LENK-SQ bioconjugates into LENK in serum. (A) Degradation over time of LENK-SQ bioconjugates constituting the NPs. Grey, yellow and orange lines represent respectively LENK-SQ Am, LENK-SQ Dig and LENK-SQ Acyl bioconjugates (B) Release kinetic of LENK from LENK-SQ NPs. Yellow and orange lines represent released LENK-spacer and LENK peptides from LENK-SQ Dig and LENK-SQ Acyl NPs respectively.

Practically, the supramolecular organization of the 3 LENK-SQ NPs was investigated using (i) Cryogenic Transmission Electron Microscopy (CryoTEM) observation, (ii) Small/Wide Angle X-Ray and Neutron Scattering (SAXS-WAXS and SANS) analysis and (iii) Synchrotron radiation circular dichroism (SRCD) analysis. Afterwards, the article examined the interaction between the LENK-SQ NPs with BSA (Bovine serum Albumin), the most abundant protein in the plasma commonly used as a model protein and also as an

efficient lipid binder[31,32], which makes it a good candidate to interact with squalene-based prodrugs. These parameters were then correlated with the corresponding analgesic profiles.

2. Materials and Methods

Preparation of LENK-SQ NPs. LENK-SQ Am, LENK-SQ Dig and LENK-SQ Acyl were all prepared using the nanoprecipitation method. Briefly, it consists in the addition of the squalene bioconjugate, dissolved in an organic solvent, to an aqueous phase. The LENK-SQ bioconjugates were first properly dissolved into pure ethanol (6 mg/ml). Then, 333 µl of this solution was added dropwise into 1 mL of milliQ water under magnetic stirring (500 rpm). The solution became spontaneously opalescent with a strong Tyndall effect, indicating the formation of nanoparticles. Ethanol was then evaporated by concentration using a Rotavapor: the pressure was slowly decreased to 43 mbar, the flask being immersed into a water-bath at 40°C. This step was carried out until the weight loss of the sample corresponded to the initial amount of ethanol used to prepare the sample. Water was then added to reach the given final bioconjugate concentration (1 to 4 mg/ml depending on the experiments). Concerning LENK-SQ Am NPs, the characterization study required more experiments than for the 2 others bioconjugates, using the same batch. For this reason, for the experiments dedicated to comparison of nanostructure and interaction with BSA, the concentration of LENK-SQ Am NPs was lower than LENK-SQ Dig or LENK-SQ Acyl NPs.

For SANS experiments, the same procedure has been followed but with D_2O instead of H_2O to increase the neutron contrast between nanoparticles and solvent. All the solutions (ethanolic and aqueous) were filtered at 0.22 µm before the nanoprecipitation process. It was not possible to formulate stable LENK-SQ Dig and LENK-SQ Acyl nanoparticles in D_2O.

The mean particle size, polydispersity index (PdI) and Zeta potential were determined at 20°C by Dynamic Light Scattering (DLS) using a Zetasizer Ultra Red (Malvern Instruments). The scattering angle was 173° and the measurements were made after 1/10 dilution of the nanoparticles' samples in milliQ water. The measurements were performed in triplicate.

Cryogenic transmission electron microscopy (cryoTEM). The morphology of the nanoparticles was observed by cryogenic transmission electron microscopy. Drops of the solutions were deposited on EM grids covered with a holey carbon film (Quantifoil R7/2) previously treated with a plasma glow discharge (5 mA, 30 s). The excess liquid on the grids

was blotted out with filter paper, and the grids were quickly immersed in liquid ethane to form a thin vitreous ice film. The whole process was performed using a Vitrobot apparatus (FEI Company). Observations were conducted at low temperature (-180 °C) on a JEOL 2010 FEG microscope operated at 200 kV. Images were recorded with a Gatan Ultrascan 2K CCD camera for the LENK-SQ Am sample and a Gatan K2 direct detection camera for the LENK-SQ Acyl and Dig samples.

Small Angle Neutron Scattering (SANS). SANS experiments were carried out on the D22 spectrometer at ILL (10.5291/ILL-DATA.9-13-1028). Samples prepared in D_2O were inserted in 1 mm Hellma quartz cells and aligned using the thermostatic sample holder with a temperature control of 20°C. The raw data were radially averaged, corrected for electronic background and empty cell, and normalized by water scattering using the LAMP software (https://www.ill.eu/users/support-labs-infrastructure/software-scientific-tools/lamp/).[33] Three configurations were used to cover a *q* range going from 0.0013 to 0.27 $Å^{-1}$ (wavelength: λ = 13 Å, sample detector distance D = 12 m, collimation: Φ = 12.8), (λ = 4.6 Å, D = 12 m, collimation: Φ = 7.8) and (λ = 4.6 Å, D = 2 m, collimation Φ = 7.8) for respectively small, medium and large angles. Typical acquisition time was from 300 s to 3600 s in function of the configurations.

Small and Wide Angle X-ray Scattering (SAXS and WAXS). Small-angle X-ray scattering patterns (SAXS) were obtained on the SWING beamline of the SOLEIL synchrotron (Saint-Aubin, France). The scattering vector range *q* of 0.002 to 2.5 $Å^{-1}$ was obtained with an energy of 16 keV and two sample-to-detector distances (6 and 0.50 m for the SAXS and the wide-angle X-ray scattering ranges, respectively). The data were recorded by a two-dimensional Eiger 4 M (Dectris) detector. Data reduction was performed using Foxtrot software (Xenocs). The samples were placed in 1.5-mm diameter glass capillaries sealed with wax. Typical acquisition sequence was 11 or 21 frames with acquisition time of 750 ms and 350 ms gap.

Synchrotron Radiation Circular Dichroism. Synchrotron radiation circular dichroism (SRCD) experiments were performed on the DISCO beamline at the SOLEIL Synchrotron (Saint Aubin, France). The samples were inserted in a CaF_2 cell with 55 µm pathlength. The raw spectra were acquired with a 1 nm spectral resolution. The spectra presented in this study were treated with CDTool software[34] that can be freely downloaded at http://www.cdtools.cryst.bbk.ac.uk/. Each is the average of three spectra. A background (water or corresponding buffer spectrum recorded under the same conditions) was subtracted.

Intensity calibration was obtained with a camphor sulfonic acid CSA scale standard sample. Finally, intensities were converted from millidegrees (θ machine units) into Δε using the formula $\Delta\varepsilon = \theta \times (0.1 \times MRW)/(3298 \times l^{*}C)$, where MRW is the mean residue weight of the chiral molecule (protein weight/number of residues = 111.12 Da for Leu-enkephalin and 114 Da for BSA), *l* is the path length of the CaF_2 cell in cm and *C* is the protein concentration in mg/ml. In some cases, we have added a smoothing function. The secondary structure analyses were performed using BestSel[35,36], a web software (https://bestsel.elte.hu/index.php).

3. Results and discussion

3. I. Characterization of the 3 LENK-SQ NPs

In a previous study,[11] 3 types of LENK-SQ NPs were designed with different analgesic profiles. It was already shown in that study that *in vitro* incubation of LENK-SQ Am NPs did not evidence the release of LENK, while LENK-SQ Acyl and LENK-SQ Dig NPs released rapidly the LENK free and LENK-Dig fragment (LENK attached to its spacer) respectively, followed by their progressive degradation over time (Figure 2). Based on the fact that, in general, an amide bond is chemically and enzymatically more stable than an ester bond,[37,38] these findings were not particularly surprising. Indeed, in the case of the LENK-SQ-Dig bioconjugate, the diglycolate spacer was attached on one side to squalene moiety by an ester bond and on the other side to the LENK through an amide bond while with the LENK-SQ-Acyl bioconjugate, both the LENK and the SQ moieties were each linked to the acylal spacer through an ester bond (Scheme 1), which is expected to be more sensitive to enkephalinases enzymes. Last, as mouse serum is particularly rich in esterases, it was expected that the release of LENK from LENK-SQ NPs mainly resulted from enzymatic hydrolysis of the ester bond.[37] However, as already explained in the introduction, based only on the nature of the linkage between LENK and SQ, it was not possible to correlate these *in vitro* experiments with the analgesic profiles *in vivo*.

Therefore, the morphology and structure of the LENK-SQ NPs were first characterized before focusing on the interaction of LENK-SQ NPs with BSA.

a) Surface charge characterization of the 3 LENK-SQ NPs

The NPs suspensions (see table 1 **nanoprecipitation batch 2023 in water) were first analyzed by DLS just after nanoprecipitation. LENK-SQ Am (1 mg/ml) and LENK-SQ-Dig

(2 mg/ml) exhibited quite the same average diameters of around 70 nm with negative zeta potentials corresponding to - 42 and - 36 mV respectively (Table 1). LENK-SQ-Acyl (2 mg/ml), were smaller with an average diameter of 46 nm and a positive zeta potential corresponding to + 42 mV. The surface charge of the NPs was attributed to the free terminal function of the peptide that was conjugated either through its N- or C- terminal site to squalene. Indeed, free N-terminal amine function led to a net positive surface charge, while free C-terminal acid function resulted in a net negative surface charge. The surface charge is a very important parameter which influences the composition of the protein corona and, in turn, strongly determines the ultimate fate of the NPs *in vivo* .[39,40] The size of NPs also plays an important role and determines the quantity of proteins adsorbed as well as the thickness of the protein corona.[41] Indeed, smaller NPs display a more curved surface compared to the larger ones, leading for each individual particle to a lower surface available for individual proteins and less accessibility to proteins due to steric effects caused by protein overcrowding. The large nanoparticles favor multilayers and conformation changes of the proteins, while monolayers are more frequently observed on small nanoparticles (< 20 nm).[42] In their review, Latreille *et al.*[42] underlined the difficulties of characterization of protein corona and protein conformation changes around large radius nanoparticles.[42] In addition, it must be kept in mind that most of these observations were obtained through the study of hard, mineral NPs and that the interaction of soft nano-assemblies, such as squalene-based nanoparticles with biological fluids, might be different. For example, we have previously demonstrated with Adenosine-squalene NPs that albumin could even extract the bioconjugates from the nanoassemblies and disassemble them, while the formation of a corona remained elusive.[29] Thus, the fact that LENK-SQ Acyl NPs were positively charged may partly explain their long-lasting analgesic effect despite the very sensitive acylal linkage.

b) Size distribution, internal nanostructure and colloidal stability of LENK-SQ Am NPs

The combination of SAXS/SANS and cryoTEM analysis is a powerful method to determine the size distribution and internal structure of self-assembling nanoparticles.[29,43] In this section, we will initiate a comparison of these three techniques on LENK-SQ Am NPs, which serve as our reference material. Subsequently, we will delve into the comparison of the three bioconjugates in the following section.

Initial observations with cryoTEM showed that SQ-LENK Am NPs were spherical and that the statistical measurement of the diameter of 39 NPs was distributed in the 15-80 nm range (Figure 3A-B). High magnification of the nanoparticles did not reveal any membrane structure nor a particularly organized inner structure.

LENK-SQ Am NPs (4 mg/ml) were further analyzed by X-ray and small-angle neutrons scattering, in water and deuterium respectively and the scattered beams were compared. As shown in Figure 3C, the scattered patterns appeared very similar, and the fits with a lognormal distribution of spheres yielded very comparable size distributions (Figure 3D) with average radii corresponding to 36.5 nm from the SAXS fit and 34.1 nm from the SANS fit, both exhibiting a polydispersity index of 0.35 nm. These size distributions were also remarkably similar to those obtained from low-statistics cryoTEM analyses, which suggests a good colloidal stability over the course of at least one month (period over which the three analyses were performed). Consequently, in the following sections, we will mainly use SAXS analysis.

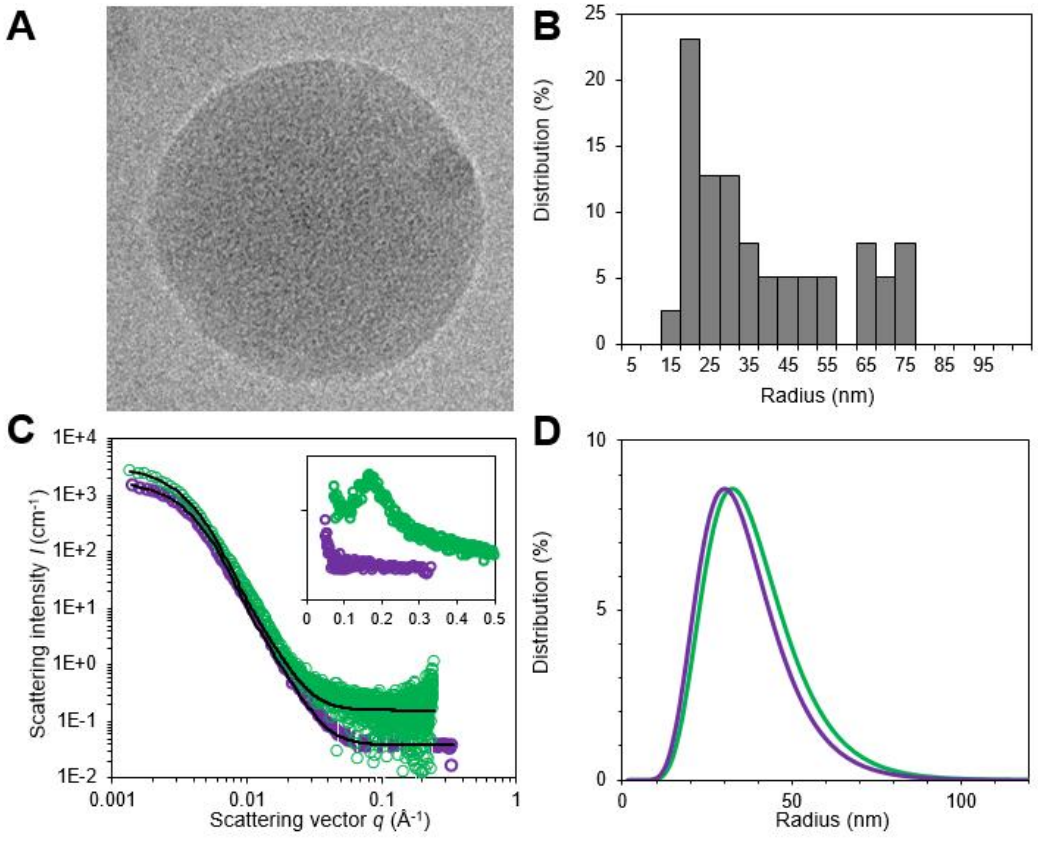

Figure 3 : A) Close-up (150 x 150 nm) of a cryoTEM image of a single LENK-SQ Am NPs (3 weeks post-nanoprecipitation). B) Size distribution (radius) obtained from the measurement of 39 nanoparticles on cryoTEM images. C) Comparison of SANS (violet circles) and SAXS (green circles) patterns of a 4 mg/ml suspension of LENK-SQ Am. SANS and SAXS analyses were performed respectively 4 days and 4 weeks post-nanoprecipitation. The fits with a model of a lognormal polydisperse spheres are plotted in black traces. Inset:

comparison of the WAXS pattern with the SANS pattern in the same q-range. D) Size distribution (radius) obtained from the corresponding fits (violet trace = distribution from SANS fit, green trace = distribution from SAXS fit). Reference to table 1 : *nanoprecipitation batch 2021 in water at 4 mg/ml

However, this case is particular considering that when the NPs components exhibit different scattering length density contrasts from SAXS and SANS, the corresponding patterns are clearly different and can provide complementary information on the inner organization of the NPs.[30] In the WAXS region (q > 0.5 Å^{-1}, see inset in Figure 3C), a weak correlation peak was detectable at q = 0.17 Å^{-1} with a FWHM of 50.8 Å^{-1}. In direct space, this data indicates electron density fluctuations on a characteristic distance of 3.7 nm inside the NPs. This could be attributed to the presence of water channels inside a sponge phase. The feature is by contrast not detected in the SANS pattern. Indeed, an x-ray beam is more focused than a neutron beam and thus provides a better resolution of the potential structural peak relative to the inner organization of the NPs (see later Figure 4C, F & I). By contrast, a brilliant synchrotron beam is much more prone to cause radiation damage to fragile organic nano-assemblies than a neutron beam.[44–46] In that respect, SAXS acquisitions were performed on the three LENK-SQ families in different points with short irradiation times to mitigate this potential risk (SI-1).

c) Comparison of the size distribution and internal structure of the three LENK-SQ NPs

The 3 LENK-SQ NPs were characterized by cryoTEM and SAXS/WAXS techniques and the results were reported in Figure 4.

First, cryoTEM allowed imaging of individual LENK-SQ NPs in hydrated conditions, thus preserving their native structure and morphology (Figure 4 A, D, and G). The three LENK-SQ NPs were found roughly spherical with diameters in the 70-150 nm range. However, LENK-SQ Dig appeared a little bit deformed and somewhat elongated (Figure 3D), which may result from a lower mechanical resistance in comparison to the two other NPs. Again, no specific or repetitive organization of the inner structure has been observed.

The analysis of LENK-SQ suspensions by SAXS (within 24 h after nanoprecipitation) evidenced the typical signature of NPs suspensions with a decrease of the scattering intensity versus the wave vector q (Figure 4 B, E, and H). In the low q-range, the intensity tends toward a plateau for the LENK-SQ Dig NPs, which agrees with non-interacting particles. However, for LENK-SQ Am and LENK-SQ Acyl NPs, the slight increase in intensity indicates a particle aggregation tendency. In the middle q-range range, the intensity can be fitted by a

model of a lognormal population of spheres whose distribution is shown in the insets in Figure 4B, E and H.

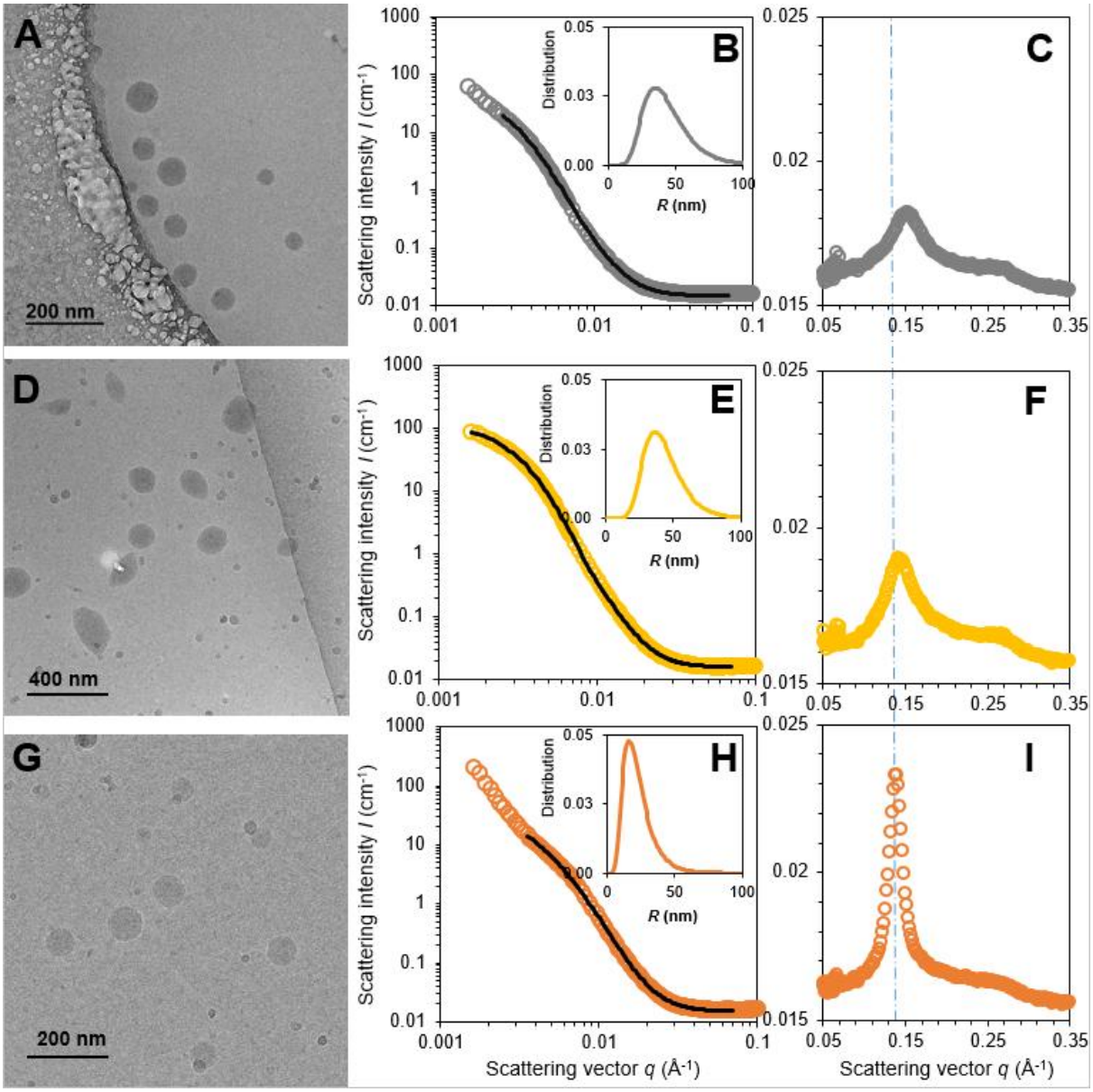

Figure 4: CryoTEM image (left panels), SAXS (center panels) and WAXS patterns (right panels) of the different bioconjugates: LENK-SQ Am (grey circles), LENK-SQ-Dig (yellow circles) and LENK-SQ Acyl (orange circles). The black traces are the fitting from lognormal distribution of polydisperse spheres. The corresponding lognormal distributions are shown in the insets. The size histograms built from measurements on cryoTEM images are shown in Figure SI-2. The WAXS patterns with Bragg peaks are shown with a linear scale. The vertical dot-dashed lines are there to visualize the slight shift of the first order position. Reference to table 1: **nanoprecipitation batch 2023 in water for all analysis except for the cryoTEM images of LENK-SQ Am obtained from * nanoprecipitation batch 2021.

The average values of radii, listed in the Table 1 along with those obtained from other analyses techniques, are of the same order of magnitude as those obtained by DLS (which were measured just after the preparation of the NPs). This highlights the small evolution of the nanoparticles diameter along the experimental time scale.

Table 1: **Summary of the different size measurement of the three types of LENK-SQ NPs with DLS, cryoTEM, SAXS and SANS.**

	LENK-SQ Am	**LENK-SQ Dig**	**LENK-SQ Acyl**
DLS†	D_{hydro} = 72 nm, PDI = 0.04** D_{hydro} = 122±22 nm, PDI = 0.08***	D_{hydro} = 73 nm, PDI = 0.01** D_{hydro} = 75±11 nm, PDI = 0.13***	D_{hydro} = 46 nm, PDI = 0.102** D_{hydro} = 120±6 nm, PDI = 0.25***
cryoTEM◊	$D_{average}$ = 73 nm* D_{median} = 57 nm* STDEV = 38 nm* (*n* = 39)	$D_{average}$ = 152 nm** D_{median} = 135 nm** STDEV = 65 nm** (*n* = 108)	$D_{average}$ = 55 nm** D_{median} = 50 nm** STDEV = 24 nm** (*n* = 69)
SAXS	$D_{average}$ = 73 nm, PDI = 0.35* $D_{average}$ = 81.2 nm, PDI = 0.38**	$D_{average}$ = 82 nm, PDI = 0.33**	$D_{average}$ = 40.4 nm, PDI = 0.46**
SANS	$D_{average}$ = 68.2 nm, PDI = 0.35*	no data	no data
ζ-potential	-42 mV** -31±10 mV***	-36 mV** -35±7 mV***	+42 mV** +33±4 mV***

†the DLS measurements yield and hydrodynamic radius, including the hydration layer around the NPs.

◊The size histograms built from measurements on cryoTEM images are shown in Figure SI-2.

*****nanoprecipitation batch 2021 in water at 4 mg/ml; ******nanoprecipitation batch 2023 in water at 1 mg/ml for LENK-SQ Am, and 2 mg/ml for LENK-SQ Dig and LENK-SQ Acyl; ***measurements from Feng *et al.*[11] with nanoprecipitation ay 4 mg/ml in dextrose 5%

Overall, the Table 1 shows a rather good agreement on the size measurements of the NPs nanoprecipitated in water. Only the LENK-SQ Dig NPs seem overestimated with CryoTEM, probably because the NPs were slightly distorted under freezing and, in fact, it was the longest axes of the elongated NPs that were measured. Regarding the variability in size distribution observed by DLS for the same types of NPs, it must be mentioned that nanoprecipitations were performed either in water or dextrose 5% at different concentrations, depending on the required experiments. Thus, the average size of the nanoparticles may vary, but always in the 50-150 nm range.

Although no internal ordering was visible on the cryoTEM images, the WAXS analysis, however, highlighted a correlation peak (table 2) (Figure 4C, F, and I) around 0.15 $Å^{-1}$ with a q^{-2} decay typical of the sponge bilayer correlation in the particles.[47] While the peaks in the LENK-SQ Am and LENK-SQ Dig are rather wide and weak, the peak in the LENK-SQ-Acyl was thinner and yielded a higher intensity, indicating a stronger organization of the bioconjugate molecules in the core of the NPs. Using the classical relation $d = 2\pi/q$ between the scattering vector *q* and the characteristic distance *d*, it can be concluded there is an average distance *d* of the order of 4-5 nm (see values reported in Table 2) between the electron-dense scatterers inside the NPs. This distance could be related to the size of water channels delimited by lipid layers. This suggests that the LENK-SQ Acyl NPs are the most hydrated and the LENK-SQ Am are the less hydrated of the series of studied NPs.

Table 2: Lorentz peak fit parameters of the correlation peak.

	LENK-SQ Am	**LENK-SQ Dig**	**LENK-SQ Acyl**
position	0.15 $Å^{-1}$	0.145 $Å^{-1}$	0.138 $Å^{-1}$
characteristic distance: *d*	4.2 nm (2021: 3.7 nm)	4.3 nm	4.6 nm
FWHM	0.051 $Å^{-1}$	0.045 $Å^{-1}$	0.021 $Å^{-1}$
correlation length: ξ	12.3 nm (2021: 5.1 nm)	14.0 nm	30.0 nm

Likewise, the relation $\xi = 2\pi/FWHM$ gives an estimate of the length over which the electron-dense scatterers lose their correlation ("correlation length", ξ) and the full width at half maximum of the peak (FWHM). This correlation length was the longest (30 nm) for the LENK-SQ-Acyl NPs, almost reaching the size of their diameter. By contrast, for LENK-SQ Am and LENK-SQ Dig, this correlation length was twice as shorter (12-14 nm), thus confirming a much less structured supramolecular organization. Overall, from this set of LENK-SQ NPs, we identified two groups based on their structural organization. In the first group comprising LENK-SQ Am and LENK-SQ Dig NPs, particles have both a weak inner order, with a high tendency towards a sponge phase organization, and a second group with LENK-SQ Acyl NPs whose inner structure is much more ordered with a tendency towards an inverse 2D hexagonal phase. Paradoxically, the water channels inside the NPs were narrower when the inner structure order was looser.

d) Conformational analysis of the LENK moiety in the 3 LENK-SQ NPs by circular dichroism

In order to monitor a possible modification of the molecular conformation of the LENK moiety within the NPs, circular dichroism (CD) analyses were performed on the 3 LENK-SQ NPs suspensions at a concentration of 2 mg/ml and compared with a single solution of the LENK peptide free at the same concentration. Although the dichroic signal was rather weak, the free LENK peptide spectrum clearly exhibited a negative band at 185 nm and two positive bands at ~200 nm and ~220 nm (Figure 5A). These features could roughly be found in the CD spectra of the NPs suspensions but with various relative intensities and sometimes a slight shift. For example, the positive band in the LENK-SQ Am spectrum was stronger than its 220 nm counterparts or its equivalent in any other spectrum. By contrast, it was absent from the LENK-SQ-Acyl spectrum.

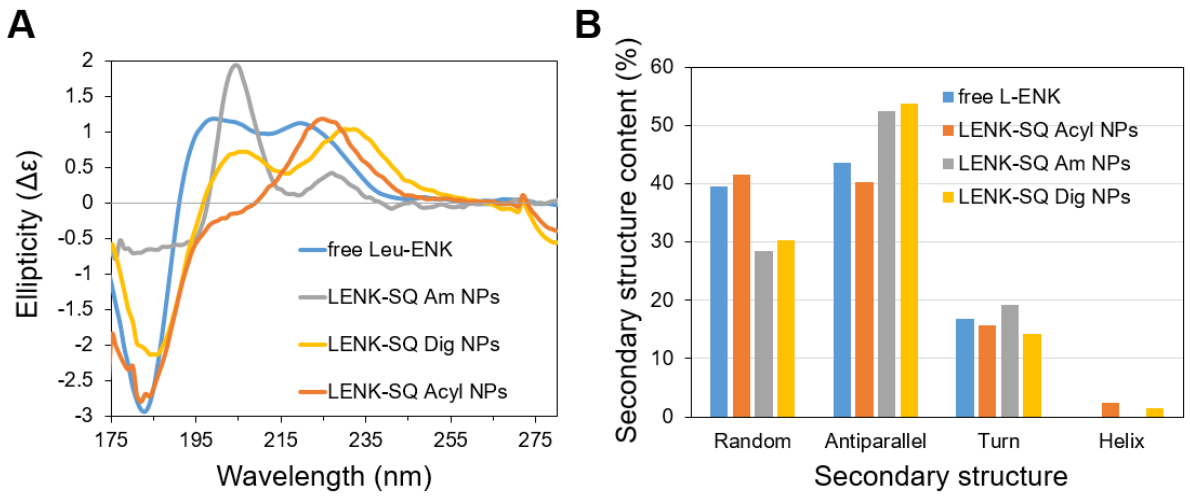

Figure 5: A) Synchrotron radiation circular dichroism spectra of the three NPs suspensions along with the spectrum of free LENK in solution (2 mg/ml). Blue trace: free LENK, grey trace: LENK-SQ Am, yellow trace: LENK-SQ Dig and orange trace: LENK-SQ Acyl. **B)** Secondary structure analysis of the spectra performed with the BestSel online software.[35,36]

The secondary structure analysis of these spectra defines two groups of NPs: a first group with LENK-SQ-Acyl whose secondary structure content was very similar to that of the free peptide and a second group with LENK-SQ Am and LENK-SQ Dig where 10% of the overall secondary structure was converted from random conformation to antiparallel β-sheet (Figure 5B). This suggests that in these LENK-SQ Am and LENK-SQ Dig nano-assembled NPs an extra hydrogen bond between peptide chains is holding the organization along with the hydrophobic interaction between lipid chains.

Overall, the physico-chemical characterization of the three LENK-SQ NPs shows that, despite strong chemical similarities between the three LENK-SQ bioconjugates that only differ in the linkage between the LENK and SQ moieties, the resulting NPs appear not strictly equivalent. Indeed, LENK-SQ-Acyl NPs exhibited specific features not shared by the other two NPs: not only they displayed a positive surface charge but they also appear to have a more ordered structural organization. Yet, they also seem to be more hydrated than the other two. In addition, the LENK-SQ Am were found to be the less hydrated NPs but also the more disordered. If we now specifically look at the conformation of the LENK peptide incorporated in the NPs, here again, the LENK-SQ-Acyl NPs stand out. Indeed, the secondary structure of the peptide moiety appeared very similar to that of the free peptide in solution, i.e., mainly random conformation (in addition to a turn and intramolecular H-bonds), while in the two other bioconjugates, a small part of this random component was transformed into a β-sheet conformation. This reduced degree of liberty could be related to the slightly more confined water channels in the LENK-SQ Am and LENK-SQ Dig NPs, comparatively to the LENK-SQ Acyl NPs. Nevertheless, the peptide conformation was only marginally modified in the three different NPs, and such a small change is unlikely enough to affect their biological activity.

3. II. Study of LENK-SQ NPs interaction with BSA

a) SAXS and WAXS analysis of LENK-SQ NPs after interaction with BSA

To better understand the behavior of the 3 LENK-SQ NPs in the blood circulation, an *in vitro* study was performed by incubating these NPs with serum albumin, which accounts for 55% of the protein content in the plasma.[48,49] The NPs were then characterized by SAXS and WAXS techniques. Figure 6 illustrates the behavior of the SAXS patterns for the 3 LENK-SQ NPs (at a fixed concentration) with increasing BSA concentrations; the curves in black correspond to the NPs suspensions free of BSA. As described above, the scattering intensities increased at scattering vectors below q = 0.02-0.01 $Å^{-1}$. By contrast, the scattering of BSA molecules, which was smaller, occurred in the 0.01-0.3 $Å^{-1}$ q-range.[50] The scattering intensity below q = 0.01 $Å^{-1}$ was, therefore, only arising from the NPs and its modification was then a direct consequence of a change in the NPs size/number/morphology, at least as long as the scattering signal was above 10 cm^{-1} (Figure 6, left panel). There was, however, an overlap between the WAXS internal structural peak of the NPs and the BSA signal (Figure 6, right panel) that rendered the analysis less straightforward and required a deconvolution of the

signals arising from the NPs structure and the BSA (which could also be modified by the interaction). In all cases, the addition of BSA induced a significant modification of the overall SAXS/WAXS signals, both by addition of a scattering signal arising from the BSA and by decreasing the scattering of the NPs.

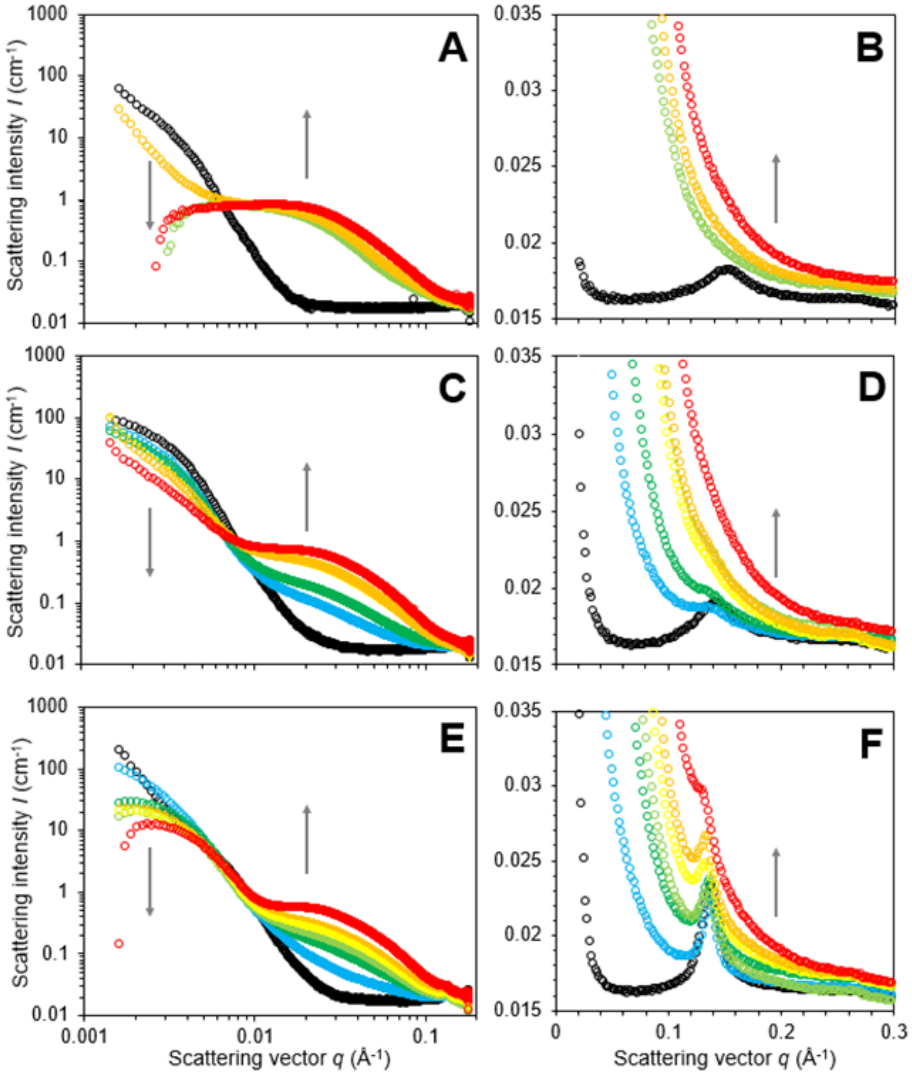

Figure 6: SAXS/WAXS patterns for the three NPs (LENK-SQ Am (A-B), LENK-SQ Dig (C-D) and LENK-SQ Acyl (E-F)) for a constant SQ concentration ([LENK-SQ Am]= 0.75 mg/ml, [LENK-SQ Dig]= 1 mg/ml, [LENK-SQ Acyl] = 1 mg/ml) and increasing BSA concentration from 1 to 10 mg/ml (black trace = NPs without BSA, blue = 1 mg/ml BSA, dark green = 2 mg/ml BSA, light green = 3 mg/ml BSA, yellow = 4 mg/ml BSA, orange = 6 mg/ml BSA and red = 10 mg/ml BSA). The left side are the SAXS patterns in logarithmic scale and the right side are the WAXS patterns in linear scale.

For LENK-SQ Am NPs (analyzed at a concentration of 0.75 mg/ml), the NPs signature at low angles decreased and even disappeared in the presence of 3 to10 mg/ml of

BSA (Figure 6 A). Taking this into account, two scenarios could be considered: either a disassembly of the NPs or, on the contrary, an expansion of the NPs volume. Generally, a significant growth of NPs induces a shift of their SAXS signatures at a lower *q*, thus leading to their destabilization, but this was not observed here. Therefore, it seems obvious that the LENK-SQ Am NPs disassembled in the presence of BSA. Of note, the Bragg peak of the NPs was not visible in the presence of BSA at a 3 mg/ml concentration, hidden by the scattering of the BSA.

For LENK-SQ Dig NPs (analyzed at a concentration of 1 mg/ml), the same trend was observed with a decrease of the NPs signature at low angle (Figure 6 C). However, the signature remained still higher than that observed with LENK-SQ Am NPs, and a continuous decrease of NPs signature with increasing BSA concentrations was observed. For the two lowest BSA concentrations (1 mg/ml and 2 mg/ml), the intensity in the low *q* range tended towards a plateau with a decrease in intensity value. This indicates a decrease of the volume fraction of these NPs, probably associated with their disassembly. With increasing the concentrations of BSA to 4 mg/ml, the decrease in intensity at low *q* was associated with a modification of the shape of the scattering curves in the low *q* range. The intensity did not tend towards a plateau but increased. The NPs shape or the interactions between the nanoparticles was, therefore, altered in the presence of BSA at concentration above 4 mg/ml. At larger *q*, the Bragg peak of the NPs was still visible at BSA concentrations of 1 and 2 mg/ml, although less intense than in the absence of BSA, while it was no more visible for higher BSA concentration (Figure 6 D). Overall, the influence of BSA on LENK-SQ Dig NPs appeared to be less important than for LENK-SQ Am NPs. However, because the concentration of LENK-SQ Am was lower than for LENK-SQ Dig (0,75 mg/ml versus 1 mg/ml), the conclusion about the effect of BSA on LENK-SQ-Am was completed by SANS analysis. Indeed, the sensitivity of SANS for lipid nano-assemblies is higher than that obtained by SAXS, due to a higher scattering length density contrast between the solvent and the squalene ($\Delta\rho$ = 6 vs 1 cm^{-2}). Figure 7 illustrates the respective strengths of SAXS and SANS when studying mixtures of LENK-SQ Am NPs and BSA. As we can see, with SANS technique (Figure 7 B), the scattering of these NPs was still perfectly detected, even at lower concentrations (0.5 mg/ml of LENK-SQ Am NPs). We retrieve the trends observed in a former study for SQ-Adenosine NPs in the presence of BSA.[29] The SANS patterns of LENK-SQ Am NPs could be fitted by combining the SANS patterns of BSA (used at the same concentration) with a fraction of the SANS patterns of LENK-SQ Am NPs at initial concentration, and the resulting coefficient allowed to quantify the disassembly of LENK-SQ

Am NPs. Hence, the volume fraction of LENK-SQ Am NPs (initially at 0.5 mg/ml) decreased by 20, 45 and 73 % when BSA concentration was equal to 3, 6 and 10 mg/ml respectively (see Figure SI-4 and Table SI-1). From SAXS (Figure 7 A), the sensitivity was not enough (at 0.75 mg/ml of LENK-SQ NPs) to quantify the percentage of the NPs disassembly.

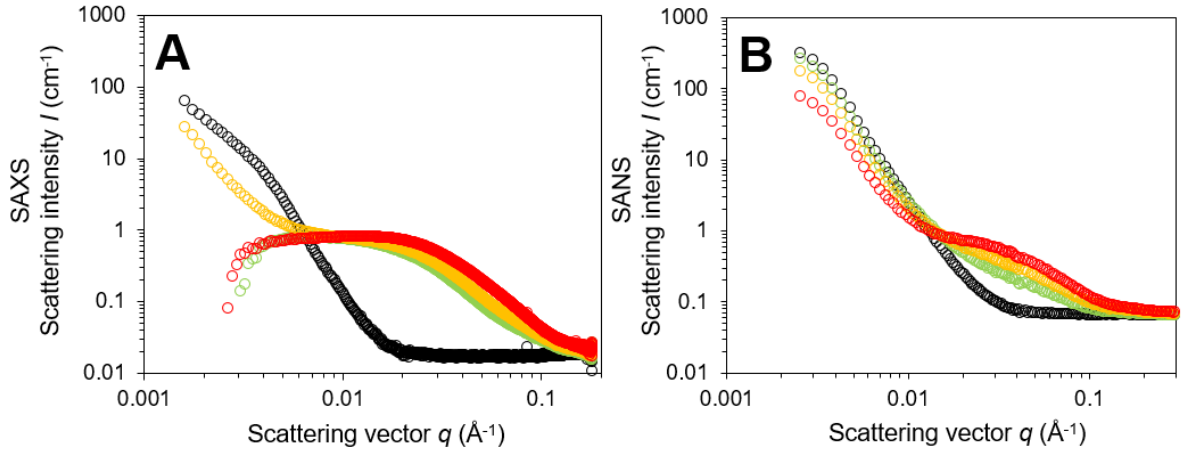

Figure 7: Comparison of SAXS and SANS patterns of LENK-SQ Am. A) SAXS patterns of SLA at 0.75 mg/ml with BSA at different concentrations (green trace = 3 mg/ml, orange trace = 6 mg/ml and red trace = 10 mg/ml). B) SANS patterns of SLA at 0.5 mg/ml with BSA at different concentrations (green trace = 3 mg/ml, orange trace = 6 mg/ml and red trace = 10 mg/ml)

For LENK-SQ-Acyl NPs, the behavior was quite different. While pristine LENK-SQ-Acyl NPs showed a slight tendency to form aggregates, as indicated by the increase signal at low *q* (black trace on Figure 6E), when BSA was added the intensity tended towards a plateau (green, orange and yellow traces on Figure 6E). This informs about a finite size of non-interacting NPs, thus suggesting that BSA stabilized the LENK-SQ-Acyl NPs. As can be seen, the value of the intensity at low *q* slightly decreased with increasing the concentrations of BSA, which suggests that the volume fraction of the LENK-SQ-Acyl NPs was slightly decreasing with the addition of BSA. Here again, this information highlights NPs disassembly, albeit lower in magnitude than for the 2 other NPs. Indeed, this time, the Bragg peak signature from the internal structure of the NPs was still visible even in the presence of high concentrations of BSA (10 mg/ml), thus suggesting that LENK-SQ Acyl NPs were much less perturbed by the presence of BSA than LENK-SQ Am and LENK-SQ Dig NPs.

b) Circular dichroism study of LENK-SQ NPs after interaction with BSA

To monitor the interaction between BSA and nanoparticles at the molecular level,[29,51] additional experiments were performed using circular dichroism spectroscopy. This methodology enables to focus on the protein counterpart involved in this interaction by tracking its conformational changes, whether the protein is adsorbed on the surface of the NPs[51] or forming a complex with the bioconjugate.[29] Indeed, LENK-SQ NPs are soft nanoassemblies that can potentially act as reservoirs from which LENK-SQ monomers can be extracted during their interaction with blood plasma components, such as BSA or lipoprotein (LDL, HDL).[29,30,52–54] In the present case, it was observed that the NPs themselves exhibited a small dichroic signal of only a few millidegrees for a LENK-SQ Am NPs solution (2 mg/ml) (Figure 5A), in comparison with that of a BSA solution (4 mg/ml) which was of the order of 50 millidegrees. The overall dichroic signal of a mixture of NPs and BSA was thus overwhelmed by that of the protein, as can be seen in Figure 8A and Figure SI 4. Figure 8A shows the CD spectra of a mixture of 4 mg/ml BSA solution in the presence of a molar excess of LENK-SQ Am NPs (1/10 : BSA/NPs molar ratio). This mixture was then subjected to a temperature ramp from 25° to 79° in steps of 3° and the thermal denaturation of BSA was then monitored and compared with that of a single BSA solution. To compare the stability of BSA in these different mixtures, the ratio of the intensities of the negative bands at 209 and 220 nm were plotted as a function of the temperature in Figure 8B. The figure shows that the denaturation of the BSA in the presence of LENK-SQ Acyl NPs follows the same trend as the free BSA (progressive increase of the I209/I220 ratio), which suggests that in this case there is no specific interaction of BSA with the LENK-SQ Acyl NPs or corresponding bioconjugates. By contrast, the denaturation curves of BSA in the presence of LENK-SQ Dig or Am NPs follow a different trend. Indeed, the I209/I220 ratios remained mostly constant up to 60° (although the absolute intensities decrease) and finally brutally dropped above 70°C. This trend suggests a possible stabilization of the BSA conformation in the presence of the LENK-SQ Dig or Am bioconjugates or NPs, thus indicating that BSA species were possibly involved in a complex with these bioconjugates.

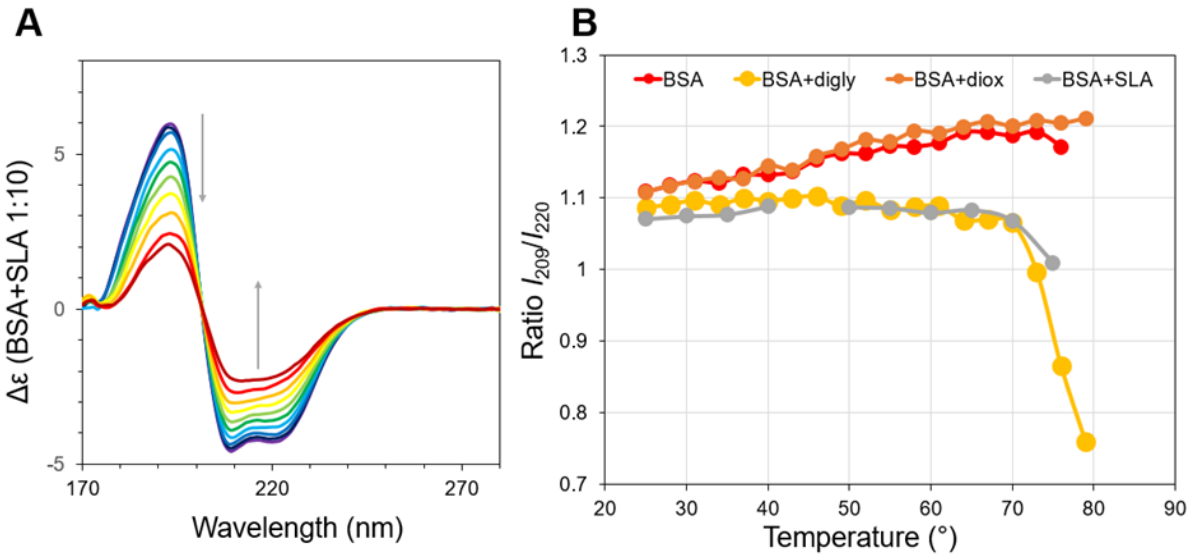

Figure 8: A) Circular dichroism monitoring of thermal denaturation of BSA in presence of an excess of LENK-SQ Am NPs (the corresponding CD graphs in the presence of LENK-SQ Dig and LENK-SQ Acyl are presented in Figure SI-3). The temperature is increased from 25° to 79° in steps of 3° (traces from violet (25°) to red (79°)). B) Plot of the CD-intensity ratio at 209 nm and 220 nm during the thermal denaturation of BSA in solution (red trace) and in the presence of LENK-SQ NPs Am (grey), Dig (yellow) and Acyl (orange), respectively.

3. III. General discussion

In this study, several factors have been identified that may affect the *in vivo* behaviour of the three LENK-SQ NPs, differing only by the nature of the chemical linkage between the neuropeptide and the squalene. The morphology and structure of the three LENK-SQ NPs were first characterized by different complementary techniques such as DLS, CryoTEM, SAXS, WAXS, SANS and CD. All the LENK-SQ NPs were found roughly spherical in a same range of size. However, the LENK-SQ NPs with an acylal spacer displayed particular features not shared by the other two LENK-SQ NPs (Am and Dig). First, LENK-SQ-Acyl NPs exhibited a positive surface charge and a reinforced inner supramolecular organization with a structure tending toward an inverse hexagonal phase, with the presence of water channels inside the NPs core. This strong structural organisation may partly explain the unpredictable long lasting analgesic effect previously observed, due to a slow release of the LENK. Indeed, it is known from literature that the internal nanostructure of self-assembled prodrugs NPs can control the drug release rates, in particular when prodrugs release depends on the activity of enzymes such as esterases as demonstrated by Sagnella et al for 5-

fluorouracil (5-FU) lipid prodrugs.[55] However, to our knowledge, the influence of the nature of the linkage of the prodrug on the internal structure of nanoassemblies and therefore its impact on drug release was never described from a physico-chemical point of view.

Additionally, the presence of a positive global charge onto the surface of the LENK-SQ-Acyl NPs (in comparison with the two other NPs exhibiting a negative charge) evidently suggested a different interaction with plasma proteins. Using BSA as a model protein, SAXS and WAXS analysis showed that LENK-SQ-Acyl NPs were less perturbed in the presence of BSA than LENK-SQ Am and LENK-SQ Dig NPs. This was confirmed by circular dichroism, which has not established a specific interaction of BSA with the LENK-SQ Acyl NPs (or corresponding bioconjugates). All this information may explain why LENK-SQ NPs with an acylal spacer did not produce the expected immediate *in vivo* analgesic effect, as anticipated by the high sensitivity of the acylal moiety to the enzymatic activation, and as also observed experimentally *in vitro* after measuring the bioconversion of the LENK-SQ Acyl prodrug in the presence of serum (Figure 2). In comparison, LENK-SQ Am and Dig presented a rather different supramolecular organization. They both exhibited a weaker inner structural order, with a high tendency to a sponge phase organization with slightly more confined water channels. Interestingly, in these NPs, an extra hydrogen bond between the peptide chains was shown to hold the organization along with the hydrophobic interaction between the SQ lipid moieties. These NPs exhibited both a negative surface charge and are more sensitive to the presence of BSA, particularly LENK-SQ Am NPs. Indeed, SAXS technique indicated that both LENK-SQ NPs disassembled in the presence of BSA, especially the NPs with amide bond. This was obviously confirmed by circular dichroism that suggested a stabilization of the BSA conformation in the presence of the LENK-SQ Am or Dig bioconjugates or NPs, by forming a complex with these prodrugs. Thus, the strong interaction of LENK-SQ Am NPs with BSA, which triggered the disassembly of the NPs provided an easier access of enzymes towards the bioconversion of the LENK-SQ Am bioconjugates, which probably explain the previously observed strong and rapid analgesic effect (Figure 1).

All these experiments emphasized the necessity to perform an in-depth physico-chemical study of the self-assembled NPs to fully understand their fate in the body and to better appreciate their pharmacological efficacy. The shape, charge, internal structure of the NPs, as well as their interaction with plasma proteins are, indeed, crucial information to better understand their activity. Beyond the disassembly phenomena of the NPs induced by the presence of protein, the crucial question of the precise mechanism of this interaction through

the formation of a protein corona requires more investigations based on molecular dynamics.[51]

4. Conclusion

The design of lipid prodrug nanomedicines with self-assembly properties represents an emerging chemotherapeutic approach for the treatment of severe diseases.[44] It is generally accepted that tailoring the chemical link of the prodrug allows to finely control the drug release profile into the body. This study shows that the supramolecular structural organization of the nanoparticles represents also a key parameter, often underestimated, which may also significantly influence the pharmacological activity. By using bovine serum albumin as a model protein and three different lipid neuropeptide prodrugs, it is shown that the structure of the resulting nanoparticles may dramatically impact the interaction with the protein corona, with the consequence to importantly affect the drug leakage and bioavailability.

Acknowledgments

This work was supported by french Research Program Agency (ANR) as part of the ‘‘Investissements d’Avenir’’ program (Labex NanoSaclay, reference: ANR-11-IDEX_0003-02 (10-LABX-0035))

We acknowledge SOLEIL (Saint Aubin, France) for provision of synchrotron radiation facilities beamtime (BAG #20201118 and proposal #20220108). We thank Dr. Thomas Bizien and Dr. Javier Perez for assistance in using the SWING beamline.
We acknowledge Zahraa AJAMI and Arthur ALLAIRE for their help during SOLEIL experiments.
We acknowledge the Institut Laue-Langevin (Grenoble, France) for provision of beamtime for the SANS experiments (Proposals 9-13-1028 and 9-13-1068). We thank Dr. Anne Martel for assistance in using the D22 beamline.

This work benefited from the use of the SasView application (http://www.sasview.org), originally developed under NSF award DMR-0520547. SasView contains code developed with funding from the European Union’s Horizon 2020 research and innovation program under the SINE2020 project, grant agreement no. 654000.

5. References

(1) Liz-Marzán, L. M.; Nel, A. E.; Brinker, C. J.; Chan, W. C. W.; Chen, C.; Chen, X.; Ho, D.; Hu, T.; Kataoka, K.; Kotov, N. A.; Parak, W. J.; Stevens, M. M. What Do We Mean When We Say Nanomedicine? *ACS Nano* **2022**, *16* (9), 13257–13259. https://doi.org/10.1021/acsnano.2c08675.

(2) Moore, T. L.; Rodriguez-Lorenzo, L.; Hirsch, V.; Balog, S.; Urban, D.; Jud, C.; Rothen-Rutishauser, B.; Lattuada, M.; Petri-Fink, A. Nanoparticle Colloidal Stability in Cell Culture Media and Impact on Cellular Interactions. *Chem. Soc. Rev.* **2015**, *44* (17), 6287–6305. https://doi.org/10.1039/C4CS00487F.

(3) Chung, H.; Kim, T. W.; Kwon, M.; Kwon, I. C.; Jeong, S. Y. Oil Components Modulate Physical Characteristics and Function of the Natural Oil Emulsions as Drug or Gene Delivery System. *J. Controlled Release* **2001**, *71* (3), 339–350. https://doi.org/10.1016/S0168-3659(00)00363-1.

(4) Apte, S. A Review of Classification of Emerging Excipients in Parenteral Medications. *Pharm. Technol.* **2003**, *27* (3).

(5) Wang, J.-J.; Sung, K. C.; Hu, O. Y.-P.; Yeh, C.-H.; Fang, J.-Y. Submicron Lipid Emulsion as a Drug Delivery System for Nalbuphine and Its Prodrugs. *J. Controlled Release* **2006**, *115* (2), 140–149. https://doi.org/10.1016/j.jconrel.2006.07.023.

(6) Couvreur, P.; Stella, B.; Reddy, L. H.; Hillaireau, H.; Dubernet, C.; Desmaële, D.; Lepêtre-Mouelhi, S.; Rocco, F.; Dereuddre-Bosquet, N.; Clayette, P.; Rosilio, V.; Marsaud, V.; Renoir, J.-M.; Cattel, L. Squalenoyl Nanomedicines as Potential Therapeutics. *Nano Lett.* **2006**, *6* (11), 2544–2548. https://doi.org/10.1021/nl061942q.

(7) Feng, J.; Lepetre-Mouelhi, S.; Couvreur, P. Design, Preparation and Characterization of Modular Squalene-Based Nanosystems for Controlled Drug Release. *Curr. Top. Med. Chem.* **2022**, *17* (25), 2849–2865.

(8) Reddy, L. H.; Dubernet, C.; Mouelhi, S. L.; Marque, P. E.; Desmaele, D.; Couvreur, P. A New Nanomedicine of Gemcitabine Displays Enhanced Anticancer Activity in Sensitive and Resistant Leukemia Types. *J. Controlled Release* **2007**, *124* (1–2), 20–27. https://doi.org/10.1016/j.jconrel.2007.08.018.

(9) Raouane, M.; Desmaele, D.; Gilbert-Sirieix, M.; Gueutin, C.; Zouhiri, F.; Bourgaux, C.; Lepeltier, E.; Gref, R.; Ben Salah, R.; Clayman, G.; Massaad-Massade, L.; Couvreur, P. Synthesis, Characterization, and in Vivo Delivery of SiRNA-Squalene Nanoparticles Targeting Fusion Oncogene in Papillary Thyroid Carcinoma. *J. Med. Chem.* **2011**, *54* (12), 4067–4076. https://doi.org/10.1021/jm2000272.

(10) Desmaële, D.; Gref, R.; Couvreur, P. Squalenoylation: A Generic Platform for Nanoparticular Drug Delivery. *J. Controlled Release* **2012**, *161* (2), 609–618. https://doi.org/10.1016/j.jconrel.2011.07.038.

(11) Feng, J.; Lepetre-Mouelhi, S.; Gautier, A.; Mura, S.; Cailleau, C.; Coudore, F.; Hamon, M.; Couvreur, P. A New Painkiller Nanomedicine to Bypass the Blood-Brain Barrier and the Use of Morphine. *Sci. Adv.* **2019**. https://doi.org/10.1126/sciadv.aau5148.

(12) Kieffer, B. L.; Gavériaux-Ruff, C. Exploring the Opioid System by Gene Knockout. *Prog. Neurobiol.* **2002**, *66* (5), 285–306. https://doi.org/10.1016/S0301-0082(02)00008-4.

(13) Janecka, A.; Fichna, J.; Janecki, T. Opioid Receptors and Their Ligands. *Curr. Top. Med. Chem.* **2004**, *4* (1), 1–17. https://doi.org/10.2174/1568026043451618.

(14) Cahill, C. M.; Holdridge, S. V.; Morinville, A. Trafficking of δ-Opioid Receptors and Other G-Protein-Coupled Receptors: Implications for Pain and Analgesia. *Trends Pharmacol. Sci.* **2007**, *28* (1), 23–31. https://doi.org/10.1016/j.tips.2006.11.003.

(15) Contet, C.; Kieffer, B. L.; Befort, K. Mu Opioid Receptor: A Gateway to Drug Addiction. *Curr. Opin. Neurobiol.* **2004**, *14* (3), 370–378. https://doi.org/10.1016/j.conb.2004.05.005.

(16) Kiritsy-Roy, J. A.; Marson, L.; Van Loon, G. R. Sympathoadrenal, Cardiovascular and Blood Gas Responses to Highly Selective Mu and Delta Opioid Peptides. *J. Pharmacol. Exp. Ther.* **1989**, *251* (3), 1096–1103.
(17) Tavani, A.; Petrillo, P.; La Regina, A.; Sbacchi, M. Role of Peripheral Mu, Delta and Kappa Opioid Receptors in Opioid-Induced Inhibition of Gastrointestinal Transit in Rats. *J. Pharmacol. Exp. Ther.* **1990**, *254* (1), 91–97.
(18) Schwartz, J.-C.; De La Baume, S.; Yi, C.-C.; Chaillet, P.; Marcais-Collado, H.; Costentin, J. Enkephalin Metabolism in Brain and Its Inhibition. *Prog. Neuropsychopharmacol. Biol. Psychiatry* **1982**, *6* (4–6), 665–671. https://doi.org/10.1016/S0278-5846(82)80166-8.
(19) Hartvig, P.; Någren, K.; Lundberg, P. O.; Muhr, C.; Terenius, L.; Lundqvist, H.; Lärkfors, L.; Långström, B. Kinetics of Four 11C-Labelled Enkephalin Peptides in the Brain, Pituitary and Plasma of Rhesus Monkeys. *Regul. Pept.* **1986**, *16* (1), 1–13. https://doi.org/10.1016/0167-0115(86)90190-4.
(20) Self, D. W.; Stein, L. Receptor Subtypes in Opioid and Stimulant Reward. *Pharmacol. Toxicol.* **1992**, *70* (2), 87–94. https://doi.org/10.1111/j.1600-0773.1992.tb00435.x.
(21) Duhem, N.; Danhier, F.; Pourcelle, V.; Schumers, J.-M.; Bertrand, O.; LeDuff, C. S.; Hoeppener, S.; Schubert, U. S.; Gohy, J.-F.; Marchand-Brynaert, J.; Préat, V. Self-Assembling Doxorubicin–Tocopherol Succinate Prodrug as a New Drug Delivery System: Synthesis, Characterization, and *in Vitro* and *in Vivo* Anticancer Activity. *Bioconjug. Chem.* **2014**, *25* (1), 72–81. https://doi.org/10.1021/bc400326y.
(22) Rodríguez-Nogales, C.; Sebastián, V.; Irusta, S.; Desmaële, D.; Couvreur, P.; Blanco-Prieto, M. J. A Unique Multidrug Nanomedicine Made of Squalenoyl-Gemcitabine and Alkyl-Lysophospholipid Edelfosine. *Eur. J. Pharm. Biopharm.* **2019**, *144*, 165–173. https://doi.org/10.1016/j.ejpb.2019.09.017.
(23) Couvreur, P.; Reddy, L. H.; Mangenot, S.; Poupaert, J. H.; Desmaële, D.; Lepêtre-Mouelhi, S.; Pili, B.; Bourgaux, C.; Amenitsch, H.; Ollivon, M. Discovery of New Hexagonal Supramolecular Nanostructures Formed by Squalenoylation of an Anticancer Nucleoside Analogue. *Small* **2008**, *4* (2), 247–253. https://doi.org/10.1002/smll.200700731.
(24) Bekkara-Aounallah, F.; Gref, R.; Othman, M.; Reddy, L. H.; Pili, B.; Allain, V.; Bourgaux, C.; Hillaireau, H.; Lepêtre-Mouelhi, S.; Desmaële, D.; Nicolas, J.; Chafi, N.; Couvreur, P. Novel PEGylated Nanoassemblies Made of Self-Assembled Squalenoyl Nucleoside Analogues. *Adv. Funct. Mater.* **2008**, *18* (22), 3715–3725. https://doi.org/10.1002/adfm.200800705.
(25) Lorscheider, M.; Tsapis, N.; Simón-Vázquez, R.; Guiblin, N.; Ghermani, N.; Reynaud, F.; Canioni, R.; Abreu, S.; Chaminade, P.; Fattal, E. Nanoscale Lipophilic Prodrugs of Dexamethasone with Enhanced Pharmacokinetics. *Mol. Pharm.* **2019**, *16* (7), 2999–3010. https://doi.org/10.1021/acs.molpharmaceut.9b00237.
(26) Mat Azmi, I. D.; Wu, L.; Wibroe, P. P.; Nilsson, C.; Østergaard, J.; Stürup, S.; Gammelgaard, B.; Urtti, A.; Moghimi, S. M.; Yaghmur, A. Modulatory Effect of Human Plasma on the Internal Nanostructure and Size Characteristics of Liquid-Crystalline Nanocarriers. *Langmuir* **2015**, *31* (18), 5042–5049. https://doi.org/10.1021/acs.langmuir.5b00830.
(27) Barauskas, J.; Cervin, C.; Jankunec, M.; Špandyreva, M.; Ribokaitė, K.; Tiberg, F.; Johnsson, M. Interactions of Lipid-Based Liquid Crystalline Nanoparticles with Model and Cell Membranes. *Int. J. Pharm.* **2010**, *391* (1–2), 284–291. https://doi.org/10.1016/j.ijpharm.2010.03.016.
(28) Bode, J. C.; Kuntsche, J.; Funari, S. S.; Bunjes, H. Interaction of Dispersed Cubic Phases with Blood Components. *Int. J. Pharm.* **2013**, *448* (1), 87–95. https://doi.org/10.1016/j.ijpharm.2013.03.016.
(29) Gobeaux, F.; Bizeau, J.; Samson, F.; Marichal, L.; Grillo, I.; Wien, F.; Yesylevsky, S. O.; Ramseyer, C.; Rouquette, M.; Lepêtre-Mouelhi, S.; Desmaële, D.; Couvreur, P.; Guenoun, P.; Renault, J.-P.; Testard, F. Albumin-Driven Disassembly of Lipidic

Nanoparticles: The Specific Case of the Squalene-Adenosine Nanodrug. *Nanoscale* **2020**, *12* (4), 2793–2809. https://doi.org/10.1039/C9NR06485K.
(30) Caillaud, M.; Gobeaux, F.; Hémadi, M.; Boutary, S.; Guenoun, P.; Desmaële, D.; Couvreur, P.; Wien, F.; Testard, F.; Massaad-Massade, L. Supramolecular Organization and Biological Interaction of Squalenoyl SiRNA Nanoparticles. *Int. J. Pharm.* **2021**, *609*, 121117. https://doi.org/10.1016/j.ijpharm.2021.121117.
(31) Peters Jr., T. 3 - Ligand Binding by Albumin. In *All About Albumin*; Academic Press: San Diego, 1995; pp 76–132. https://doi.org/10.1016/B978-012552110-9/50005-2.
(32) Fasano, M.; Curry, S.; Terreno, E.; Galliano, M.; Fanali, G.; Narciso, P.; Notari, S.; Ascenzi, P. The Extraordinary Ligand Binding Properties of Human Serum Albumin. *IUBMB Life* **2005**, *57* (12), 787–796. https://doi.org/10.1080/15216540500404093.
(33) Richard, D.; Ferrand, M.; Kearley, G. J. Analysis and Visualisation of Neutron-Scattering Data. *J. Neutron Res.* **1996**, *4* (1), 33–39. https://doi.org/10.1080/10238169608200065.
(34) Lees, J. G.; Smith, B. R.; Wien, F.; Miles, A. J.; Wallace, B. A. CDtool—an Integrated Software Package for Circular Dichroism Spectroscopic Data Processing, Analysis, and Archiving. *Anal. Biochem.* **2004**, *332* (2), 285–289. https://doi.org/10.1016/j.ab.2004.06.002.
(35) Micsonai, A.; Wien, F.; Kernya, L.; Lee, Y.-H.; Goto, Y.; Réfrégiers, M.; Kardos, J. Accurate Secondary Structure Prediction and Fold Recognition for Circular Dichroism Spectroscopy. *Proc. Natl. Acad. Sci.* **2015**, *112* (24). https://doi.org/10.1073/pnas.1500851112.
(36) Micsonai, A.; Wien, F.; Bulyáki, É.; Kun, J.; Moussong, É.; Lee, Y.-H.; Goto, Y.; Réfrégiers, M.; Kardos, J. BeStSel: A Web Server for Accurate Protein Secondary Structure Prediction and Fold Recognition from the Circular Dichroism Spectra. *Nucleic Acids Res.* **2018**, *46* (W1), W315–W322. https://doi.org/10.1093/nar/gky497.
(37) Simões, M. F.; Valente, E.; Gómez, M. J. R.; Anes, E.; Constantino, L. Lipophilic Pyrazinoic Acid Amide and Ester Prodrugs. *Eur. J. Pharm. Sci.* **2009**, *37* (3–4), 257–263. https://doi.org/10.1016/j.ejps.2009.02.012.
(38) Wong, P. T.; Choi, S. K. Mechanisms of Drug Release in Nanotherapeutic Delivery Systems. *Chem. Rev.* **2015**, *115* (9), 3388–3432. https://doi.org/10.1021/cr5004634.
(39) Monopoli, M. P.; Åberg, C.; Salvati, A.; Dawson, K. A. Biomolecular Coronas Provide the Biological Identity of Nanosized Materials. *Nat. Nanotechnol.* **2012**, *7* (12), 779–786. https://doi.org/10.1038/nnano.2012.207.
(40) Walczyk, D.; Bombelli, F. B.; Monopoli, M. P.; Lynch, I.; Dawson, K. A. What the Cell "Sees" in Bionanoscience. *J. Am. Chem. Soc.* **2010**, *132* (16), 5761–5768. https://doi.org/10.1021/ja910675v.
(41) Piella, J.; Bastús, N. G.; Puntes, V. Size-Dependent Protein–Nanoparticle Interactions in Citrate-Stabilized Gold Nanoparticles: The Emergence of the Protein Corona. *Bioconjug. Chem.* **2017**, *28* (1), 88–97. https://doi.org/10.1021/acs.bioconjchem.6b00575.
(42) Latreille, P.-L.; Le Goas, M.; Salimi, S.; Robert, J.; De Crescenzo, G.; Boffito, D. C.; Martinez, V. A.; Hildgen, P.; Banquy, X. Scratching the Surface of the Protein Corona: Challenging Measurements and Controversies. *ACS Nano* **2022**, *16* (2), 1689–1707. https://doi.org/10.1021/acsnano.1c05901.
(43) Schuldes, I.; Noll, D. M.; Schindler, T.; Zech, T.; Götz, K.; Appavou, M.-S.; Boesecke, P.; Steiniger, F.; Schulz, P. S.; Unruh, T. Internal Structure of Nanometer-Sized Droplets Prepared by Antisolvent Precipitation. *Langmuir* **2019**, *35* (42), 13578–13587. https://doi.org/10.1021/acs.langmuir.9b00944.
(44) Hopkins, J. B.; Thorne, R. E. Quantifying Radiation Damage in Biomolecular Small-Angle X-Ray Scattering. *J. Appl. Crystallogr.* **2016**, *49* (3), 880–890. https://doi.org/10.1107/S1600576716005136.
(45) Stachowski, T. R.; Snell, M. E.; Snell, E. H. SAXS Studies of X-Ray Induced Disulfide Bond Damage: Engineering High-Resolution Insight from a Low-Resolution Technique. *PLOS ONE* **2020**, *15* (11), e0239702. https://doi.org/10.1371/journal.pone.0239702.

(46) Jeffries, C. M.; Graewert, M. A.; Svergun, D. I.; Blanchet, C. E. Limiting Radiation Damage for High-Brilliance Biological Solution Scattering: Practical Experience at the EMBL P12 Beamline PETRAIII. *J. Synchrotron Radiat.* **2015**, *22* (2), 273–279. https://doi.org/10.1107/S1600577515000375.
(47) Lei, N.; Safinya, C. R.; Roux, D.; Liang, K. S. Synchrotron X-Ray-Scattering Studies on the Sodium Dodecyl Sulfate–Water–Pentanol–Dodecane L 3 Sponge Phase. *Phys. Rev. E* **1997**, *56* (1), 608–613. https://doi.org/10.1103/PhysRevE.56.608.
(48) Issaq, H. J.; Xiao, Z.; Veenstra, T. D. Serum and Plasma Proteomics. *Chem. Rev.* **2007**, *107* (8), 3601–3620. https://doi.org/10.1021/cr068287r.
(49) Anderson, N. L.; Anderson, N. G. The Human Plasma Proteome. *Mol. Cell. Proteomics* **2002**, *1* (11), 845–867. https://doi.org/10.1074/mcp.R200007-MCP200.
(50) Heinen, M.; Zanini, F.; Roosen-Runge, F.; Fedunová, D.; Zhang, F.; Hennig, M.; Seydel, T.; Schweins, R.; Sztucki, M.; Antalík, M.; Schreiber, F.; Nägele, G. Viscosity and Diffusion: Crowding and Salt Effects in Protein Solutions. *Soft Matter* **2012**, *8* (5), 1404–1419. https://doi.org/10.1039/C1SM06242E.
(51) Sanchez-Guzman, D.; Giraudon--Colas, G.; Marichal, L.; Boulard, Y.; Wien, F.; Degrouard, J.; Baeza-Squiban, A.; Pin, S.; Renault, J. P.; Devineau, S. *In Situ* Analysis of Weakly Bound Proteins Reveals Molecular Basis of Soft Corona Formation. *ACS Nano* **2020**, *14* (7), 9073–9088. https://doi.org/10.1021/acsnano.0c04165.
(52) Sobot, D.; Mura, S.; Yesylevskyy, S. O.; Dalbin, L.; Cayre, F.; Bort, G.; Mougin, J.; Desmaële, D.; Lepetre-Mouelhi, S.; Pieters, G.; Andreiuk, B.; Klymchenko, A. S.; Paul, J.-L.; Ramseyer, C.; Couvreur, P. Conjugation of Squalene to Gemcitabine as Unique Approach Exploiting Endogenous Lipoproteins for Drug Delivery. *Nat. Commun.* **2017**, *8* (1), 15678. https://doi.org/10.1038/ncomms15678.
(53) Gaudin, A.; Yemisci, M.; Eroglu, H.; Lepetre-Mouelhi, S.; Turkoglu, O. F.; Dönmez-Demir, B.; Caban, S.; Sargon, M. F.; Garcia-Argote, S.; Pieters, G.; Loreau, O.; Rousseau, B.; Tagit, O.; Hildebrandt, N.; Le Dantec, Y.; Mougin, J.; Valetti, S.; Chacun, H.; Nicolas, V.; Desmaële, D.; Andrieux, K.; Capan, Y.; Dalkara, T.; Couvreur, P. Squalenoyl Adenosine Nanoparticles Provide Neuroprotection after Stroke and Spinal Cord Injury. *Nat. Nanotechnol.* **2014**, *9* (12), 1054–1062. https://doi.org/10.1038/nnano.2014.274.
(54) Gaudin, A.; Tagit, O.; Sobot, D.; Lepetre-Mouelhi, S.; Mougin, J.; Martens, T. F.; Braeckmans, K.; Nicolas, V.; Desmaële, D.; de Smedt, S. C.; Hildebrandt, N.; Couvreur, P.; Andrieux, K. Transport Mechanisms of Squalenoyl-Adenosine Nanoparticles Across the Blood–Brain Barrier. *Chem. Mater.* **2015**, *27* (10), 3636–3647. https://doi.org/10.1021/acs.chemmater.5b00267.
(55) Sagnella, S. M.; Gong, X.; Moghaddam, M. J.; Conn, C. E.; Kimpton, K.; Waddington, L. J.; Krodkiewska, I.; Drummond, C. J. Nanostructured Nanoparticles of Self-Assembled Lipid pro-Drugs as a Route to Improved Chemotherapeutic Agents. *Nanoscale* **2011**, *3* (3), 919–924. https://doi.org/10.1039/C0NR00781A.